Assessing the performance limits of internal coronagraphs through end-to-end modeling

John E. Krist[a], Ruslan Belikov[b], Laurent Pueyo[c], Dimitri P. Mawet[d], Dwight Moody[a], John T. Trauger[a], Stuart B. Shaklan[a]

[a]Jet Propulsion Laboratory/California Inst. of Technology, 4800 Oak Grove Drive, Pasadena, CA 91109 (USA)

[b]NASA Ames Research Center, Moffett Field, CA 94035 (USA)

[c]Space Telescope Science Institute, 3700 San Martin Drive, Baltimore, MD 21218 (USA)

[d]European Southern Observatory, Alonso de Córdova 3107, Vitacura, 763 0355, Santiago, Chile

ABSTRACT

As part of the NASA ROSES Technology Demonstrations for Exoplanet Missions (TDEM) program, we conducted a numerical modeling study of three internal coronagraphs (PIAA, vector vortex, hybrid bandlimited) to understand their behaviors in realistically-aberrated systems with wavefront control (deformable mirrors). This investigation consisted of two milestones: (1) develop wavefront propagation codes appropriate for each coronagraph that are accurate to 1% or better (compared to a reference algorithm) but are also time and memory efficient, and (2) use these codes to determine the wavefront control limits of each architecture. We discuss here how the milestones were met and identify some of the behaviors particular to each coronagraph. The codes developed in this study are being made available for community use. We discuss here results for the HBLC and VVC systems, with PIAA having been discussed in a previous proceeding.

Keywords: Coronagraph

1. INTRODUCTION

1.1 Coronagraphic imaging of extrasolar planets

The imaging of mature (>1 Gyr) extrasolar planets requires the ability to separate the light of something that is $\sim 10^{-9}$ (Jupiter twin) or $\sim 10^{-10}$ (Earth twin) as bright as its star in reflected light (young giant planets are easier as they glow in the infrared with contrasts of $10^{-4} - 10^{-5}$). The planet and star are separated by a fraction of an arcsecond. To deal with the instrumental glare, a coronagraph may be used to suppress the diffracted light from a telescope's obscurations while scattered light from optical fabrication errors can be reduced using one or more deformable mirrors.

A wide variety of coronagraphic techniques exist or have been proposed. Some operate by modifying the distribution of light in a pupil (e.g., shaped pupils[1], phase-induced amplitude apodization[2] (PIAA)), others by altering the light at an intermediate focus (e.g., hybrid bandlimited coronagraph[3] (HBLC), vector vortex coronagraph[4] (VVC)). Variations of these can include the use of deformable mirrors to help control diffraction, even in the absence of any wavefront aberrations. There are also interferometric options (e.g., visible nuller[5]). The specific designs for each can be adjusted to optimize:

- Inner working angle (IWA): the angle from the star at which the transmission of a point source has been reduced 50% relative to the maximum field transmission.
- Field coverage: some coronagraphs (e.g., shaped pupil) can be tailored to reduce diffraction in a limited portion of the field, with trade-offs with IWA, throughput, and contrast.
- Throughput: the transmission through the coronagraph, as set by stops, apodization masks, or focal plane masks, may often be traded against IWA and contrast
- Low order aberration sensitivity: the IWA, contrast, and throughput may be traded off against the ability to reject changes in low order aberrations such as tip, tilt, focus, coma, astigmatism, etc.

The current states of the different coronagraphic techniques vary considerably. Some have been evaluated in testbeds in near-flight configurations and conditions and have achieved (or nearly so) the required contrasts in broadband light. Others have been tested in simplified versions and only in monochromatic light. Some exist only as models. So far, none has demonstrated with actual hardware the 10^{-10} contrast over a ~20% wavelength bandpass necessary to characterize an Earth twin (by contrast here, we mean that a background speckle created by optical errors and diffraction is equal in brightness to a planet of this flux ratio relative to the star).

Until real hardware exists that provides 10^{-10} contrast, we must utilize numerical models to evaluate the performance limits and behaviors of the coronagraphic techniques. Such models are required for optimizing the design, demonstrating its expected performance with realistic optics, and creating the system response matrices used for wavefront control in both simulated and real systems. This requires accurate wavefront propagators and representations of the coronagraphic components.

1.2 TDEM study and milestones

To verify that the wavefront propagators are accurate to the contrast limits being considered and to understand the wavefront control behaviors of certain coronagraphs, we undertook a study within the NASA ROSES Technology Demonstration for Exoplanet Missions (TDEM) program. It had two milestones, the definitions and subsequent attainments of which were reviewed and approved by the NASA Exoplanet Exploration Program Technology Assessment Committee:

1. Identify, implement in code, and verify efficient numerical methods for representing wavefront modification by the Hybrid Band-Limited Coronagraph (HBLC), the Vector Vortex Coronagraph (VVC), and the Phase-Induced Amplitude Apodization (PIAA) coronagraph that are accurate to 1% or better relative to the mean field contrast for contrasts down to 10^{-10} as judged against the results from more robust, though slower, methods.
2. Using the algorithms established in Milestone 1, assess the performances of HBLC, VVC, and PIAA coronagraphs via end-to-end modeling in a realistic and aberrated optical system with wavefront control to achieve a numerically-predicted mean contrast of 10^{-10} within a $r = 2.5 – 18\ \lambda/D$ radian annulus centered on the star integrated over a ~20% ($\lambda = 500 – 600$ nm) bandpass.

The milestone definitions and results of this study are presented in more detail in the final results reports[6]. This work was an extension of an earlier, more cursory study[7].

Milestone 1 defined and verified the algorithms that would be used in Milestone 2 to evaluate the performance of each specific coronagraph design in an aberrated system. Because the end-to-end modeling in Milestone 2 would involve thousands of propagations through the optical system (for generating the deformable mirror response matrix and for iterative wavefront control), the methods established in Milestone 1 had to be as efficient as possible while still being accurate enough to capture the behavior of the coronagraph.

The Milestone 1 efficiency was judged by the total amount of time it took to compute the effects of individually pushing each active DM actuator on each of the two 46 × 46 DMs at each of five sampling wavelengths (500, 525, 550, 575, 600 nm), for a total of about 18,100 full propagations from the DM to the image plane. Assuming a perfectly symmetrical system and making use of the eight-fold symmetry of the deformable mirror, the time limit was set at 48 hours on a modern multiprocessor workstation. This number of propagations would be required to construct the DM response matrix used for wavefront control. The accuracy metric was the root-mean-square of the difference of the electric fields produced by the efficient method (E_{eff}) and a more rigorous, slower reference method (E_{ref}), as measured within the specified field around the occulted source and expressed in terms of contrast:

$$accuracy = RMS\left(\left|E_{eff} - E_{ref}\right|^2\right) \Big/ \max\left(PSF\right)$$

Dividing the RMS of the intensity of the field differences by the peak value of the unocculted stellar PSF converts the result into contrast. The accuracy requirement was evaluated using aberrations that produced image fields with mean contrasts of 10^{-5} and 10^{-10}.

1.3 Propagators and verifying their accuracies

To assess the impact of errors on each optical surface, the numerical wavefront propagator must be able to compute the diffraction of the beam from optic to optic, including those not at a pupil or a focus (which are easily handled by single Fourier transform between pupil and focus). This allows the effects of phase-to-amplitude (and vice-versa) transitions (Talbot effect) and out-of-plane vignetting to be included. This requires a combination of near and far field diffraction algorithms.

The freely-available PROPER library[9] for IDL (Interactive Data Language) was the baseline propagation system for this study. It implements the angular spectrum and Fresnel propagators, includes a model of a deformable mirror with actuator influence functions, can create synthetic surface error maps using power spectral density specifications, and can generate complex obscuration patterns. The propagators are based on the Fourier transform (but are more complex than the single Fourier transform commonly used for Fraunhoffer diffraction). In cases where the available PROPER routines were not sufficient, custom routines written in IDL or C were used (e.g., propagation between the PIAA remapping optics or the representation of the small opaque spot at the center of the vector vortex focal plane mask).

Ideally, one would compare computed results to those obtained in the real world, such as from a testbed, to determine the accuracy of the computations. At the 10^{-10} contrast levels of concern here the unknown differences between the real optical system and the model would dominate the errors rather than computational ones. Instead, one must compare results from a practical (fast) algorithm to those from a reference one that is generally considered highly accurate but is likely extremely slow.

Verifying S-Huygens as a "practical" reference algorithm against Rayleigh-Sommerfeld

Our base reference method of propagation was brute-force numerical integration of the Rayleigh-Sommerfeld diffraction equation, which we assumed to be "perfect". It was much too slow to be a practical reference algorithm for anything other than a single-step propagation of a simple wavefront. For multiple-surface systems and arbitrarily-aberrated input wavefronts the S-Huygens method[10] was used as the reference. S-Huygens makes more approximations to diffraction computation than Rayleigh-Sommerfeld but fewer than the propagators used in PROPER. It is a one-dimensional propagator (radial vector of a 2-D wavefront) and can be used on circularly-symmetric wavefronts with high resolution. By decomposing the wavefront into a sufficient number of azimuthal harmonic basis functions, it can also be used for arbitrary two-dimensional wavefronts[11].

To verify the use of S-Huygens as the practical reference, we compared its results to those generated by Rayleigh-Sommerfeld. Each method was used to propagate a circularly-symmetric aberrated wavefront (circular phase ripples) between two PIAA optics (remapping and phase correction mirrors). The aberrations were chosen to produce a 10^{-10} mean contrast field at final focus between r = 2.5 and 18 λ/D. Afterwards the PIAA propagation, the wavefronts were multiplied by a greyscale apodizer and then propagated to focus using Hankel transforms. The Rayleigh-Sommerfeld calculation took 31 hours on a 256 processor system with 6.4 billion samples over the surface of the 1st optic (M1) and just a single radial cut on the 2nd. S-Huygens took 70 seconds on an 8-core workstation using parallelized code with 45,000 points along the radius of M1 (because a completely symmetrical system was used, only one S-Huygens vector needed to be calculated). Assuming the Rayleigh-Sommerfeld results were exact, the accuracy of S-Huygens was 0.04% (Figure 1) as calculated by the previously defined equation. S-Huygens was thus considered a valid reference algorithm against which to judge other methods.

Verifying PROPER against S-Huygens

The accuracy of the PROPER routines was derived against S-Huygens. Each method was used to propagate a circularly-aberrated input wavefront (for 10^{-10} contrast) through an entire simple, bandlimited Lyot coronagraphic system (including collimating and focusing optics). Based on these results, the accuracy of PROPER is 0.6% (Figure 2) when using a grid size of 2048 × 2048 with the beam at the entrance pupil spanning ¼ the diameter of the grid.

Verifying PASP against S-Huygens

The PIAA coronagraph optics compress the beam to create an apodized pupil. The spacing between rays becomes non-uniform during propagation and the resulting phase differences large, invalidating the use of the usual Fourier-based methods (as does the high curvature change at the edge of the PIAA optics). A different algorithm, PIAA Angular Spectrum Propagator (PASP)[12,13], can be used between the PIAA optics. It separately propagates each spatial frequency

component of the field, accounting for remapping. This algorithm was described in detail in our previous report[8] that detailed the results of the PIAA evaluations.

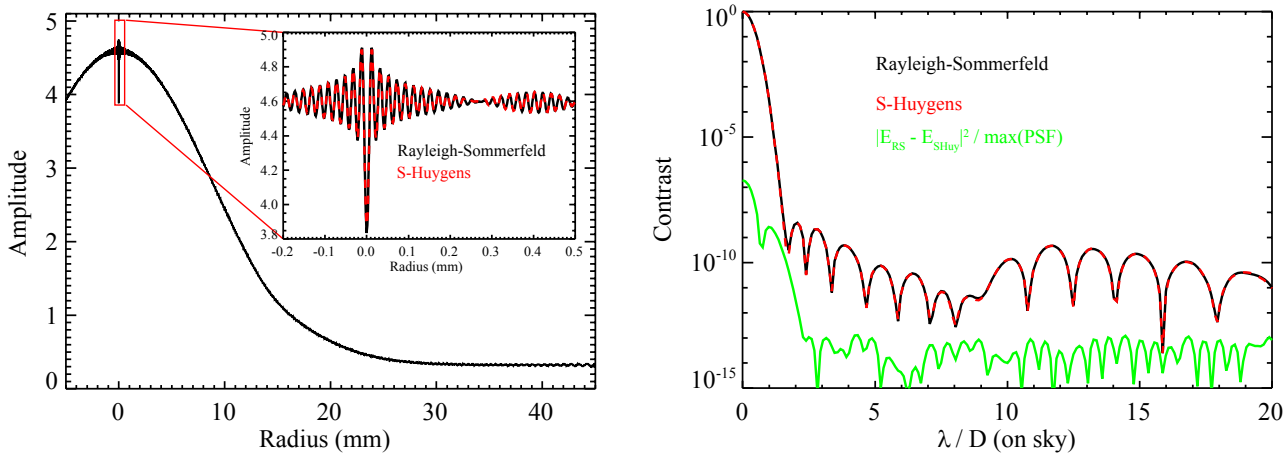

Figure 1. Comparisons of the propagation between two PIAA optics using Rayleigh-Sommerfeld and S-Huygens. (Left) The amplitude at the PIAA M2 optic. The pupil remapping by the M1 optic creates an apodized beam. (Right) The intensity at the focus of the system. The green line shows the difference between the two computed electric fields converted to intensity contrast.

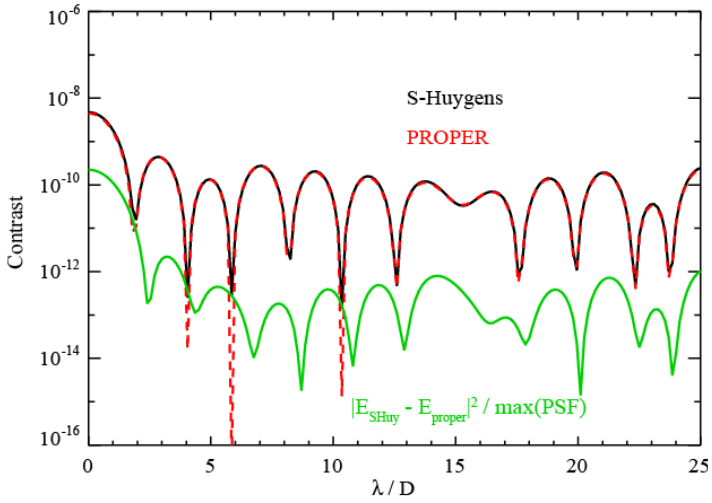

Figure 2. Plots of the ~10^{-10} contrast bandlimited Lyot coronagraph image fields calculated by PROPER and S-Huygens. The intensity contrast of the difference between the electric fields is also plotted.

1.4 Defining the model system

The common optical elements

The three model coronagraphs shared a common front end optical system starting with a 1.5 m diameter primary mirror, secondary and fold mirrors, a collimator, and two 46 × 46 actuator deformable mirrors placed in sequence and separated by 1.0 m. The two DMs, with one at a pupil, allowed both phase and amplitude errors to be corrected in a 360º region centered on the star. The HBLC and VVC utilized the same back end system (Figure 3) after the 2nd DM that consisted of an optic to focus the beam onto a focal plane mask, after which a collimator reimaged the pupil onto a Lyot stop

mask. Afterwards, the beam was focused onto the detector. In the case of PIAA, after the 2nd DM an optic created a pupil image on the 1st PIAA mirror (M1), which remapped the pupil onto the 2nd PIAA optic (M2) that corrected for the induced phase error. Another optic then reimaged the pupil onto an apodizing mask, after which another focused the beam onto an occulter at the PIAA intermediate focus, where most of the star's light was removed. The beam was then sent to a duplicate of M2 and then to M1 (this reverse-order PIAA system restored the original wavefront mapping and avoided image distortion) and then to an optic that focused onto the detector. There were some flat fold mirrors included to fit the layout into a realistic volume (the layouts are based on the ACCESS concept design study).

In the Milestone 2 step, all of the optical surfaces had synthetic phase (polishing, figuring) errors and amplitude (coating) errors appropriate to the optic type and dimension. The 2-D error maps were realizations of power spectral density specifications derived from real optics. The phase wavefront errors ranged from 1.5 nm RMS (fold mirror) to 8.3 nm RMS (primary). Measured error maps of a real set of PIAA optics were used for the PIAA simulations. The deformable mirrors were represented using a measured Xinetics actuator influence function, which is provided by PROPER.

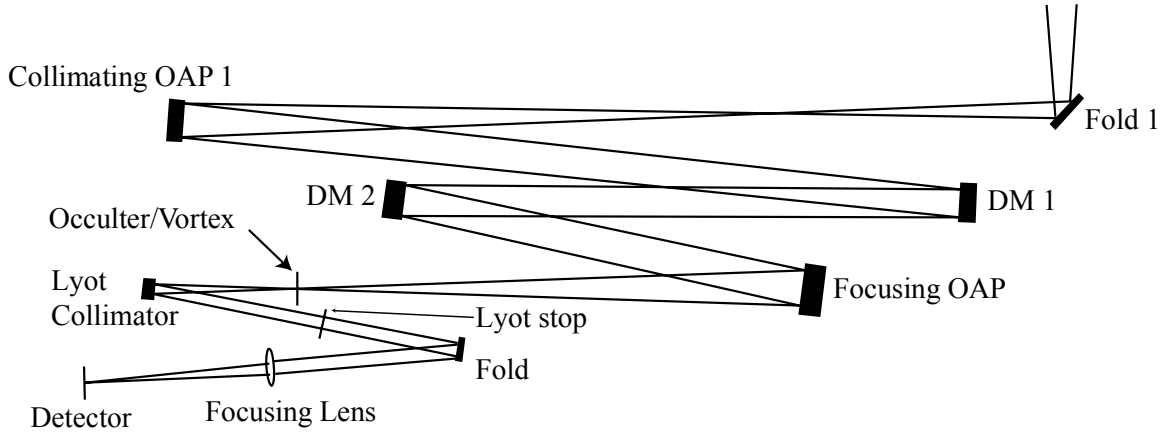

Figure 3. Schematic optical layout for the HBLC/VVC. Not shown are the telescope primary and secondary mirrors that feed Fold 1 in the upper right.

Wavefront control

In Milestone 2 the systems were placed in the aberrated system and the DMs used to control the wavefront errors, creating a zone of suppressed speckles from $r = 2.5 - 18\ \lambda/D$. The Electric Field Conjugation[14] (EFC) method was used to compute the DM settings given the measured field at the final image plane. The computed, complex-valued field was used directly, without any indirect derivation of it that would be required in a real system. EFC requires a DM response matrix that describes how the field changes with a piston of each actuator (and at each wavelength). This matrix is computed by propagating a poke of each actuator through the system (a model is necessary to generate this whether it is used in a simulation or in a real system). One of the critical parameters in EFC is the regularization value. We derived the optimal one for each coronagraph by running separate control cases.

The field at the image plane was "sensed" and controlled at 5 wavelengths evenly sampling the 500 – 600 nm bandpass. The mean contrast was evaluated using the average of the 5 monochromatic fields.

2. HYBRID BAND-LIMITED CORONAGRAPH (HBLC)

The HBLC[3] is a variation on the classical Lyot coronagraph that uses a small, opaque occulting spot in an intermediate focal plane to mask the core of the stellar PSF and an aperture (Lyot) stop in a subsequent pupil plane to block most of the remaining diffracted light. The HBLC replaces the spot with specifically-tailored amplitude-and-phase-modulating,

variable-thickness, patterned coatings. The graded amplitude transmission coating is usually a metal on top of which a patterned dielectric is applied. By modifying both the amplitude and phase in a controlled manner, and using the known material properties (indices of refraction, etc.) the HBLC focal plane mask can control wavelength-dependent transmission variations inherent in any real material as well as increase the throughput by allowing for a slightly more open Lyot stop. Even greater improvement can be achieved by modifying the wavefront with one or more deformable mirrors. The coatings and DM settings can be simultaneously optimized to produce a high-contrast field with specified inner and outer radii over a given bandpass.

The HBLC used in our simulations included the effects of coating-induced, wavelength-dependent phase and amplitude variations based on real material properties as calculated with standard thin film equations. This was a realistic design that could be used in an actual system and whose performance should closely match the predictions (excluding any mask deposition errors). The HBLC was composed of a patterned mask at an intermediate focus (Figure 4), a Lyot stop mask at a subsequent pupil plane, and control with the deformable mirrors. The DM (Figure 5) and focal plane mask patterns were optimized for an unaberrated system over r = 2.5 – 18 λ/D using an iterative method. Note that the DMs were an integral part of diffraction control, even in a perfect system; the patterns were later altered to correct for wavefront errors in an aberrated system. The focal plane mask used nickel and cryolite coatings with spatially-variable thicknesses to produce amplitude and phase modulations (Figure 4). The Lyot stop had an opening 60% the diameter of the beam, and it had a central obscuration 10% of the beam diameter (this spot was found to provide additional diffraction suppression when using the DMs). This HBLC configuration provided a mean contrast of 3.7×10^{-11} over the target field in an unaberrated system (Figure 6).

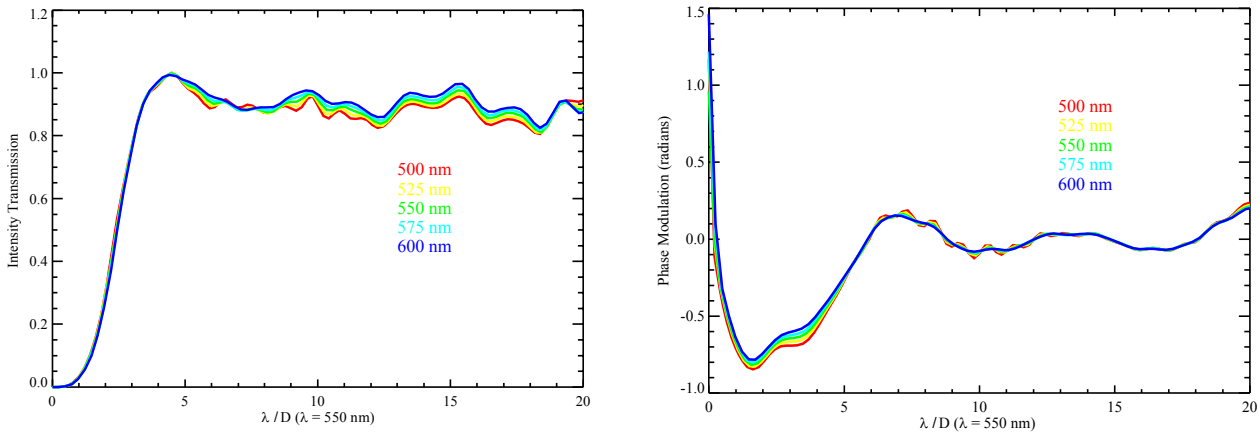

Figure 4. The HBLC focal plane mask intensity transmission (left) and phase modulation (right) used in this study. The wavelength dependence is based on thin film calculations using the properties of nickel and cryolite.

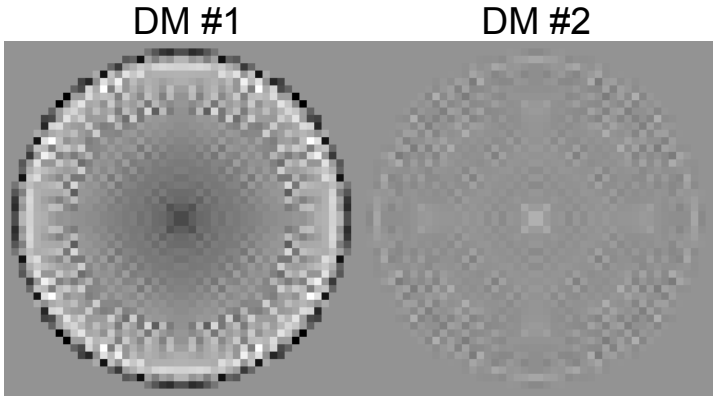

Figure 5. The initial HBLC deformable mirror settings used in this study, optimized for an unaberrated system.scaled. Shown scaled between -10.2 nm to +6.4 nm in piston.

2.1 HBLC Milestone 1 results

The HBLC did not require any special propagation algorithms or "tricks" to represent it in the numerical simulations since it simply modified the phase and amplitude with relatively smooth patterns. There was, in essence, no reference algorithm result to which a faster algorithm could be compared. For the HBLC Milestone #1 accuracy requirement, we relied on the demonstrated accuracy of the PROPER propagation algorithms.

We compared results (Figure 7) from different computational grid sizes (4096 × 4096 & 2048 × 2048) and corresponding samplings at the focal plane mask (0.079 & 0.157 λ/D, respectively, with 322 pixels across the pupil in both cases). We created a two-dimensional, isotropically-scattering, synthetic primary mirror phase map that provided a contrast floor of ~10^{-5} (low contrast case) and ~10^{-10} (high contrast case) with the default layout. The accuracies for both contrast levels, based on the differences between the 2K and 4K grids, were about the same, ~7×10^{-14} (Figure 8). It is likely that some numerical artifacts cancel out. The execution time to compute the DM response matrix as specified in the Milestone 1 requirement was 8.3 hours using 2K grids.

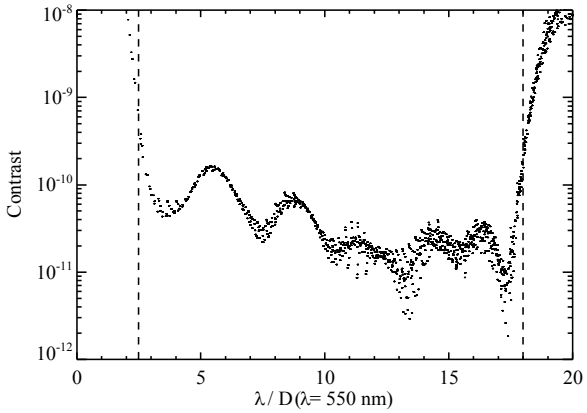

Figure 6. Radial profile of the HBLC coronagraphic field expressed as contrast for an unaberrated system over λ = 500 – 600 nm.

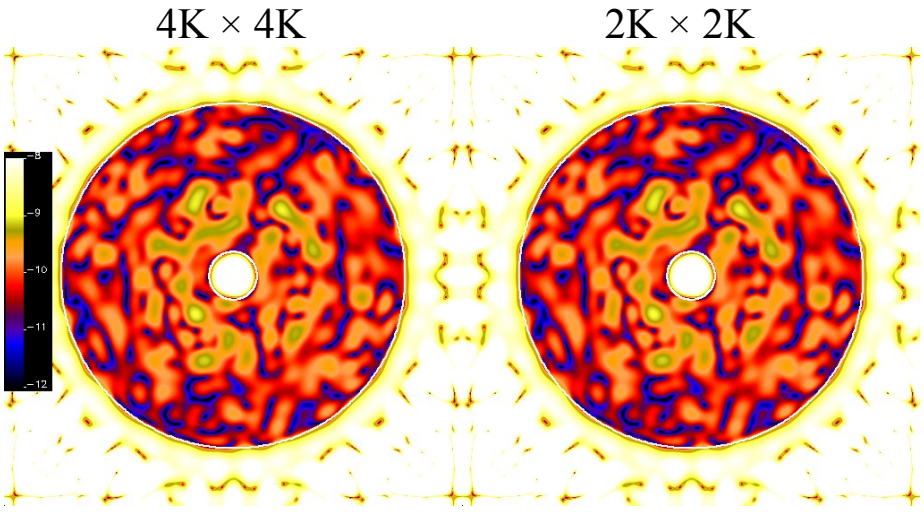

Figure 7. Monochromatic (550 nm) contrast maps for HBLC Milestone 1 simulation runs (1.1×10^{-10} mean contrast) using 4K × 4K arrays (left) and 2K × 2K arrays (right). The contrast evaluation region of r = 2.5 - 18 λ/D is marked with circles. The colorbar indicates $\log_{10}$(contrast) and ranges from 10^{-12} up to 10^{-8}.

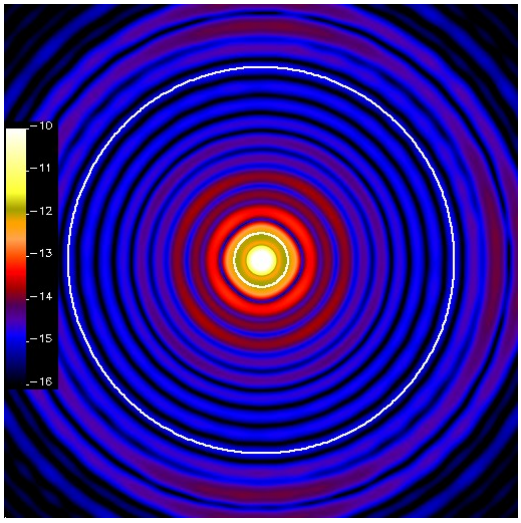

Figure 8. Difference between the 4K × 4K and 2K × 2K electric fields (10^{-10} contrast), displayed as contrast. The contrast evaluation region of r = 2.5 - 18 λ/D is marked with circles. The colorbar indicates $\log_{10}$(contrast) and ranges from 10^{-16} up to 10^{-10} (different scaling from contrast maps above).

2.2 HBLC Milestone 2 results

Trial EFC runs used different regularization values in the DM response matrix. There appeared to be a "sweet spot" using a regularization of 0.5×10^{-5}. Lower regularization values (less actuator damping) provided rapid improvements in the first few iterations but the solution would eventually diverge. A higher value (more damping) slowed the convergence rate. After 150 iterations, a regularization value of 1.0×10^{-5} reached mean contrasts (Figure 9) of 2.4×10^{-10} and 9.7×10^{-11} (for r = 2.5-3.5 λ/D, 2.5-18 λ/D, respectively). After only 50 iterations, a regularization value of 0.5×10^{-5} provided contrasts of 2.2×10^{-10} and 9.3×10^{-11} for the same annuli, which we adopted here. Because it produced the best contrast over the full field after some experimentation, we chose to use uniform weighting over a 2.2 – 18 λ_c/D annulus (the contrast was still evaluated over 2.5 – 18 λ_c/D). The target dark hole contained 7596 pixels and there were 1804 active actuators on each DM. The DM response matrix for 5 wavelengths was 2.1 GB in size. As shown in Figure 10, there is considerable variation in contrast with wavelength. With an ideal coronagraph, one might expect that the contrast would be best near the central wavelength and degrade away from it. However, the combination of the wavelength-dependent amplitude-and-phase-modifying mask and DM settings in the HBLC results in a different behavior.

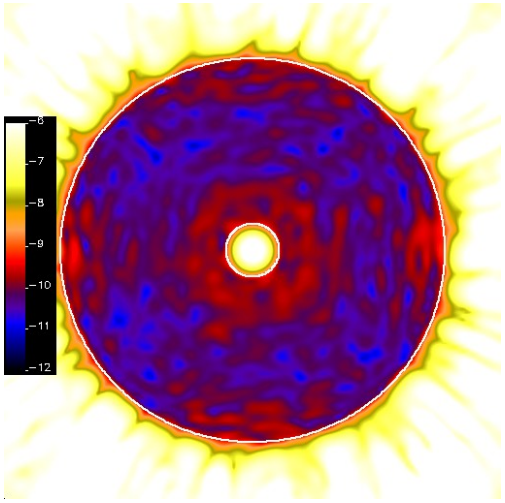

Figure 9. Final broadband contrast over the field achieved using the HBLC. Log_{10}(contrast) is shown on the color scale. The inscribed circles mark the r = 2.5 and 18 λ/D boundaries of the contrast measurement region. The mean contrast in this region is 9.3×10^{-11}. The residual structure is largely due to the wavelength-dependent coating behavior included in the HBLC mask representation.

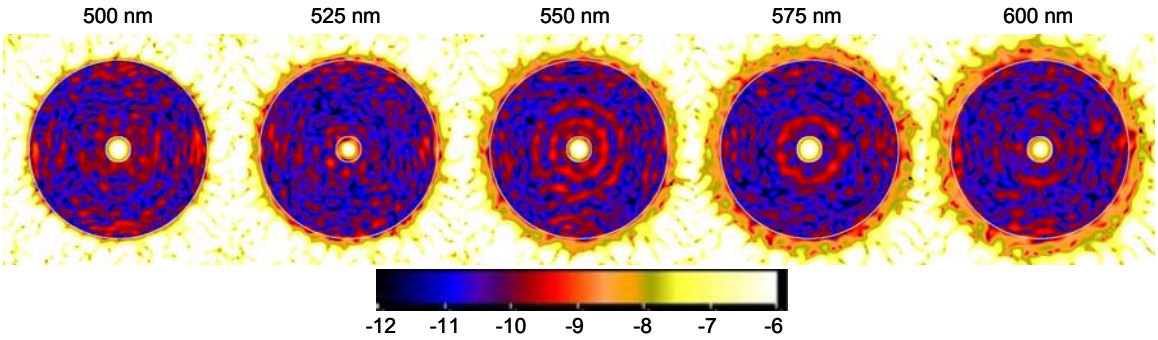

Figure 10. Final HBLC broadband contrast decomposed into monochromatic contrasts over the field. Log_{10}(contrast) is shown on the color scale (note that the contrast range is different here than for the other contrast maps in order to emphasize the variations with wavelength). The inscribed circles mark the r = 2.5 and 18 λ/D boundaries of the contrast measurement region. At the central wavelength (550 nm), the mean contrast is 9.4×10^{-11} over the dark hole.

3. VECTOR VORTEX CORONAGRAPH (VVC)

An optical vortex is created using a mask that introduces an azimuthally-varying phase shift to the wavefront, creating a "phase screw" with a singularity at the center. This results in self-interference as the wavefront propagates, forming a dark central hole in the beam at some distance from the mask. An optical vortex can be used in a Lyot coronagraph by placing a vortex-generating mask at an intermediate image plane that results in a dark central hole at a subsequent pupil plane, where a Lyot stop is placed. The advantages of an optical vortex coronagraph are that it can provide imaging very close to the star (< 2 λ/D) and has high throughput (>90%) due to a relatively wide-open Lyot stop.

Previous vortex masks were transmissive, stepped spiral patterns etched into substrates. They suffered from manufacturing defects due to the imperfect singularity at the center of the spiral and the small, nanometer-scale steps required to produce an approximation to a smooth phase ramp. They were also inherently chromatic. A new technique[4] has been developed that creates a "geometrical" phase spiral by manipulating the polarization of incoming light with novel coatings made of hardened birefringent liquid crystal polymers (LCPs). This *vector vortex* is essentially a rotationally symmetric halfwave plate (HWP) providing a geometrical phase shift that applies opposite phase screws to the two orthogonal circular polarization states. In the vector vortex, for a linearly polarized input field (or for natural light projected onto a linear basis), the rotationally symmetric HWP rotates the polarization vector. The definition of circular polarization is a linear polarization rotating at the angular frequency ω (equal to that of the electromagnetic field); a rotation $\varphi = 2\theta$ of the polarization vector is strictly equivalent to a phase delay. If, at any given point in space, the polarization vector is rotated, it implies that the given circular polarization has acquired a geometric phase ramp $e^{i\varphi} = e^{i2\theta}$. The term φ thus represents both an angle and a phase – hence the term "geometrical" phase.

The VVC focal plane mask used in these simulations had a charge of 4 (the resulting phase spiral rotates by $4 \times 2\pi$ radians), resulting in 4th order aberration rejection. An opaque circular spot of r = 0.25 λ_c/D at the center of the mask covered the "confusion zone", the region where, in a real mask, there would be large fabrication errors near the central singularity. A simple, circular Lyot stop was used at the reimaged pupil plane after the VVC mask with a clear aperture of 90% the diameter of the beam.

The broadband performance of a mask with less than 3 layers would be poor (~10^{-4} - 10^{-8} contrast) due to "chromatic leakage". A real mask would require 5 layers of polymer and operate in a single polarization channel (as we assumed in all of our simulations). Such a design would ideally create a contrast floor of <10^{-12} (this does not include reflections/scattering from interference effects, which have not been computed). We assumed that we were using a 5 layer mask, and because the predicted leakage term was far below our contrast requirement, we did not explicitly include it in our simulations.

3.1 Representation of the VVC

Breaking down the Jones matrix

The action of the vector vortex coronagraph (VVC) on the input vectorial wavefront W^i is rigorously represented by the following Jones matrix product:

$$\begin{bmatrix} W_L^o(r,\theta,\lambda) \\ W_R^o(r,\theta,\lambda) \end{bmatrix} = \begin{bmatrix} L(r,\theta,\lambda) & V(r,\theta,\lambda)e^{il\theta} \\ V(r,\theta,\lambda)e^{-il\theta} & L(r,\theta,\lambda) \end{bmatrix} \times \begin{bmatrix} W_L^i(r,\theta,\lambda) \\ W_R^i(r,\theta,\lambda) \end{bmatrix}$$

As stated in the white paper, a single polarization at a time will be analyzed, which simplifies the equation as follows:

$$\begin{aligned} \begin{bmatrix} W_L^o(r,\theta,\lambda) \\ W_R^o(r,\theta,\lambda) \end{bmatrix} &= \begin{bmatrix} L(r,\theta,\lambda) & V(r,\theta,\lambda)e^{il\theta} \\ V(r,\theta,\lambda)e^{-il\theta} & L(r,\theta,\lambda) \end{bmatrix} \times \begin{bmatrix} W_L^i(r,\theta,\lambda) \\ 0 \end{bmatrix} \\ &= \begin{bmatrix} L(r,\theta,\lambda) \times W_L^i(r,\theta,\lambda) \\ V(r,\theta,\lambda)e^{-il\theta} \times W_L^i(r,\theta,\lambda) \end{bmatrix} \\ &= \begin{bmatrix} L \times W \\ VVC \times W \end{bmatrix} \end{aligned}$$

In conclusion, the propagation through the VVC requires two main propagations, adding up incoherently: (1) the *VVC* term that will itself be broken down (see below) to represent the action of the opaque spot covering the central region of disorientation and (2) the leakage term. The chromatic leakage term *L* transmits a fraction of the incoming light without phase modification but with the amplitude modification induced by the opaque spot.

Action of the VVC in the perfect case

For a perfect VVC case (circular filled uniform pupil without aberration), the field in the pupil after the vortex focal plane mask is:

$$E_{pup} = FT[E \times VVC(l)] = HT_i[J_1] = \begin{cases} 0 & r < R_{pup}; l = 2,4,... \\ f(r) & r > R_{pup} \end{cases}$$

The action of the vortex on a perfect field E_{perf} at focus corresponds to a Hankel transform ($HT[]$) of the l_{th} order of the Bessel J_1 function. This transform has analytical solutions, known as the Weber-Schafheitlin integral, which reduces to the Sonine integral in the $l=2$ case[15]. The final rigorous analytical result of these integral solutions is that the energy inside the pupil downstream from the vortex is 0 for non-zero, even values of the *topological charge l*.

Superposition principle applied to the VVC

Now in the real world, nothing is perfect, and both the wavefront and the VVC are affected by systematic errors. The superposition principle allows rigorous decomposition of these errors linearly. The aberrated system field at the vortex plane, *E,* can be decomposed into the sum of a perfect field, E_{perf}, and an aberrated one, E_{ab}:

$$E = E_{perf} + E_{ab}.$$

Both of which correspond to the Fourier transform of a perfect wavefront at a pupil and the aberrated one:

$$W = W_{perf} + W_{ab}.$$

The action of a real world VVC_{ab} (VVC_{perf} + *central opaque spot S*) can be decomposed into the difference of a perfect VVC_{perf}, whose mathematical properties with a perfect wavefront are well known (see here above), and a finite one limited to the spot area:

$$VVC = (VVC_{perf} - VVC_{spot})$$

The superposition principle allows us to break down the action of an imperfect vortex on an imperfect wavefront, as follows

$$\begin{aligned} E \times VVC &= (VVC_{perf} - VVC_{spot}) \times (E_{perf} + E_{ab}) \\ &= (VVC_{perf} \times E_{perf}) + (VVC_{perf} \times E_{ab}) - (VVC_{spot} \times E_{perf}) - (VVC_{spot} \times E_{ab}) \end{aligned}$$

Evaluation of the first term

The first term, bearing a large fraction of the incoming beam energy (in the high Strehl ratio regime), *cancels out inside the pupil geometric area* (cf. the mathematical demonstration in the perfect case), which allows us to avoid computing it uselessly and be confronted to the well-know aliasing error of the vortex coronagraph representation at the very center (where most of the energy is). Outside of the pupil the light is masked by the Lyot stop.

For this term, the efficient method simply consists of considering this term as being 0. The reference method is analytical and gives 0 as well. The match is therefore perfect, *by definition*.

Our representation of the vortex boils down to propagating differential terms (2, 3, & 4) only, using the perfect vortex solution for the dominant (1st) one. However, leaving out this main term, which carries most of the energy, does not capture the effect of downstream aberrations. Therefore, to represent the low-level interactions between the 1st vortex term and errors on the OAP between the mask and the Lyot stop, one must carry out the propagation of the "vortexified field" ($E_{perf} \times VVC_{perf}$) from the mask, through the relay optic, and on to the Lyot stop.

The numerical representation of the vortex mask is generated by computing a phase ramp on a grid 5× larger on each side than the wavefront array (e.g., a 10K × 10K array for a 2K × 2K grid). This subsampled grid is then block averaged (real and imaginary parts separately) down to the default sampling. This method produces a good, but not perfect, representation of the vortex mask. When it is multiplied by the perfect field at focus and propagated to a pupil, aliasing and Fourier transform artifacts introduce energy inside the pupil interior, when it should be zero.

To avoid these numerical aliasing problems specific to the 1st term (and affecting low spatial frequencies), one can propagate the $E_{perf} \times VVC_{perf}$ field to the Lyot stop, zero-out the pupil interior, and then propagate back to the focal plane, using the result for future propagations. Because Fresnel algorithms are used, the field at the focus has a phase term introduced by the focusing optic, so a simple Fourier transform cannot be used to go back and forth between the focal and pupil planes. Instead, one must do a full propagation from focus to the collimator, apply a positive lens, propagate to the Lyot stop and zero out the interior, then propagate backwards to the collimator, apply a negative lens, and then back to focus. This only has to be done once per wavelength and the result stored, since the 1st term does not change.

Generally speaking an optical system could be designed in such a way that the number of relay optics is reduced to the only required OAP. This optic would be sufficiently far from the mask, hence close enough to the pupil so that the dark

hole is nearly fully formed, making the effect of surface errors nearly irrelevant after filtering by the Lyot stop. A non-telecentric system could also be constructed so that the pupil is formed after the focal plane mask without any intervening optics.

Evaluation of the second term

The second term can be propagated using the conventional FFT-based technqiues, aliasing (sampling artifacts) errors being negligible where the aberrations are (further away from the center of the vortex).

Evaluation of the third and fourth term

The third term can be very accurately represented using partial Fourier transforms, e.g. the matrix Fourier transform[16] (MFT); we only need to evaluate the effect of the mask in a very limited area (the small spot that covers alignment errors at the center of the vortex mask). This computation can be done once per wavelength, and stored for subsequent use. The perfect field at focus is Fourier transformed to a virtual pupil plane, then it is transformed back to focus using the MFT to create a very highly sampled field only within the region of the spot. This is multiplied by the vortex phase ramp and then transformed back to the virtual pupil using another MFT. The result is then Fourier transformed back to focus with the original field sampling and stored for subsequent use. We have verified that the spot, given its small size (diameter = 0.5 λ/D) has no influence on the aberrated field (verified down to about 10^{-19} for a 10^{-10} nominal contrast), so the fourth term can be neglected.

3.2 VVC Milestone 1 results

There is no known analytical method for the propagation of an aberrated field through a vector vortex to serve as a reference algorithm to determine the accuracy of the methods used here. Instead, to estimate the accuracy we ran separate simulations using different array sizes (4096 × 4096 & 2048 × 2048) and corresponding beam/grid diameter ratios (0.0625 & 0.125, respectively; the pupil size is 256 pixels across in each case). The VVC chosen for these simulations had a central opaque spot 0.5 λ/D in diameter. We used the phase map defined earlier to provide a contrast floor of 10^{-5} (low contrast case) and 10^{-10} (high contrast case).

The accuracy of the 2K grid computations, compared to those using 4K grids, was 7.2×10^{-12} for the 10^{-5} contrast field (~0% error) and 2.6×10^{-15} for the 10^{-10} contrast field (also ~0% error). Because the accuracies derived from the array size comparison were better than those established for PROPER, we used the PROPER accuracies (0.6%) as the Milestone #1 metric for the VVC. Figures 11 and 12 show the computed images and differences for the 10^{-10} contrast fields. The DM matrix test took 15.7 hours, so the efficient VVC propagation algorithms met the Milestone #1 efficiency and accuracy requirements.

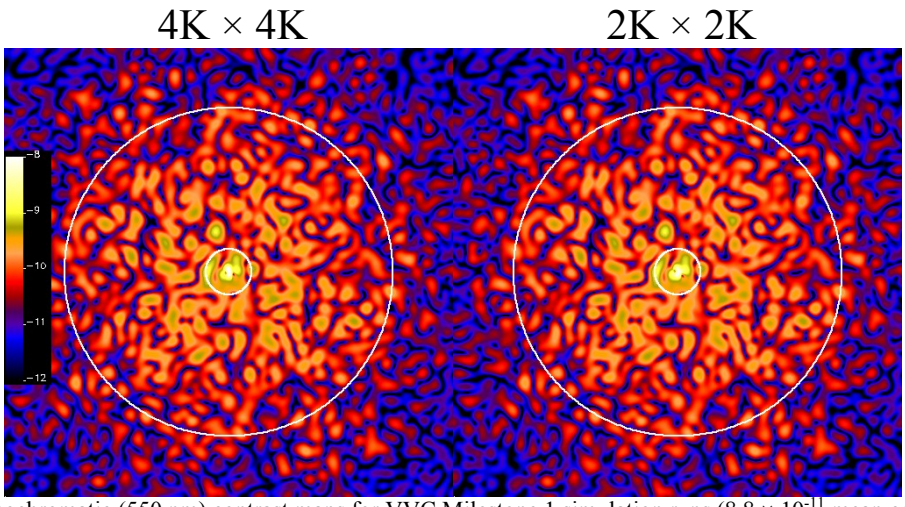

Figure 11. Monochromatic (550 nm) contrast maps for VVC Milestone 1 simulation runs (8.8×10^{-11} mean contrast) using 4K × 4K arrays (left) and 2K × 2K arrays (right). The contrast evaluation region of r = 2.5 - 18 λ/D is marked with circles. The colorbar indicates $\log_{10}$(contrast) and ranges from 10^{-12} up to 10^{-8}.

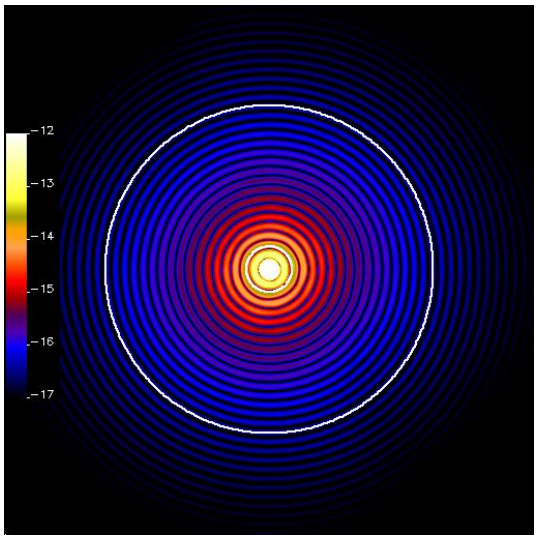

Figure 12. Difference between the 4K × 4K and 2K × 2K electric fields, displayed as contrast. The contrast evaluation region of r = 2.5 - 18 λ/D is marked with circles. The colorbar indicates $\log_{10}$(contrast) and ranges from 10^{-17} up to 10^{-12} (different from contrast maps above). The asymmetry in this residual map is due to the action of the opaque spot, which injects diffracted starlight enhancing the anti-symmetric cross-terms in the vortex.

3.3 VVC Milestone 2 results

We ran EFC on the VVC system using an empirically optimized DM response matrix regularization of 0.5×10^{-5} with a uniform weighting of 1.0 over r = 0.9 – 18 λ_c/D and 0.2 for r < 0.9 λ_c/D. After 25 iterations of EFC we reached mean contrasts of 6.0×10^{-12} over r = 2.5 – 18 λ_c/D (easily meeting the Milestone #2 requirement) and 1.5×10^{-11} over r = 2.5 – 3.5 λ_c/D (Figure 13). Unlike the HBLC, the contrast is best at the central wavelength (Figure 14). This difference is likely due to the representation of the mask being wavelength independent (excluding the fact that the central spot does not scale with wavelength). If a more realistic representation of the VVC mask were to be used (i.e., one including interference effects between coating layers), then the wavelength dependence would likely differ.

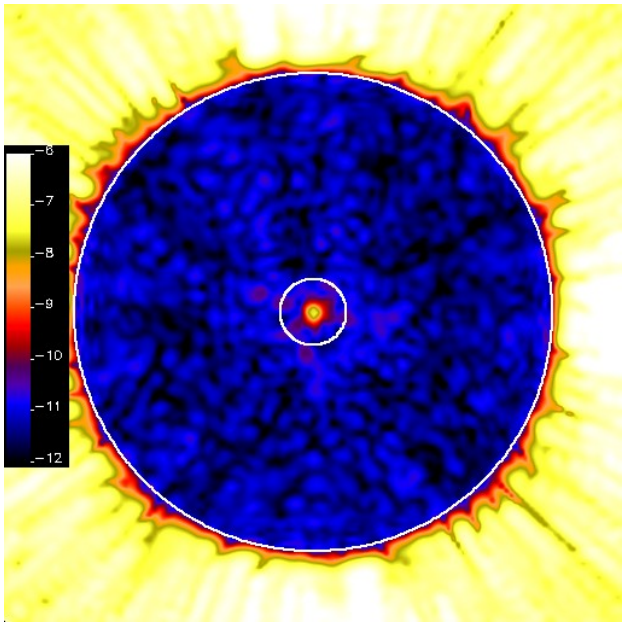

Figure 13. Final broadband contrast over the field achieved using the VVC. Log_{10}(contrast) is shown on the color scale. The mean contrast in the dark hole region is 6.0×10^{-12}. It is possible that if coating-dependent thin-film effects, including interference, were included, there would be a greater, non-uniform level of residuals, like those seen for the HBLC or PIAA.

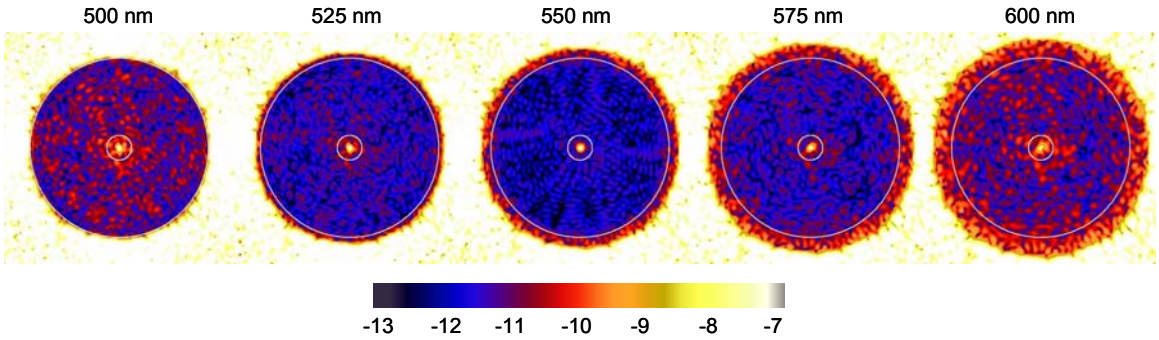

Figure 14. Final VVC broadband contrast decomposed into monochromatic contrasts over the field. Log_{10}(contrast) is shown on the color scale (note that the contrast range is different here than for the other contrast maps in order to emphasize the variations with wavelength). The inscribed circles mark the r = 2.5 and 18 λ/D boundaries of the contrast measurement region. At the central wavelength (550 nm), the mean contrast is 1.8×10^{-12} over the dark hole.

3.4 Future VVC work

Our results here show that there are no show-stoppers in the fundamental VVC design that would prevent reaching 10^{-10} contrast. However, the system used here was essentially perfect, with no errors in the vortex mask and no wavelength-dependent phase and amplitude dispersions introduced by the coatings. More work is needed to implement such errors, though they would likely be heavily dependent on particular fabrication methods. So far, the VVC has not been developed as much as HBLC or PIAA, and it requires more time to mature.

During our experiments, we concluded that for the particular VVC propagation technique we used (specifically, propagating the effect of the occulting spot) to be accurate, it was necessary to not have any optics between the focal plane mask and the subsequent collimating mirror. This prevents light near the center of the beam from being scattered by surfaces before the vortex has had a chance to form and clear out the center.

4. CONCLUSIONS

We have shown that the HBLC and VVC systems can be efficiently and accurately represented in terms of wavefront propagation. Both systems are fundamentally capable of achieving 10^{-10} mean contrast in a realistically aberrated system. We note that implementation of the VVC in our study avoided polarization effects by assuming a single polarization channel. Also, we assumed a 5 layer design that theoretically provides better than 10^{-10} control of chromatic leakage.

ACKNOWLEDGEMENTS

This work was performed at the Jet Propulsion Laboratory/California Inst. of Tech. and NASA Ames Research Center as part of NASA ROSES 09-TDEM09-0017.

REFERENCES

[1] Carlotti, A., Vanderbei, R., and Kasdin, N. J., "Optimal pupil apodizations of arbitrary apertures for high-contrast imaging", Optics Express, 19, 26796 (2011).
[2] Guyon, O., Pluzhnik, E., Galicher, R., Martinache, F., Ridgway, S., and Woodruff, R., "Exoplanet Imaging with a Phase-Induced Amplitude Apodization Coronagraph", Astrophysical Journal 622, 744 (2005).
[3] Moody, D., Gordon, B., and Trauger, J., "Design and demonstration of hybrid Lyot coronagraph masks for improved spectral bandwidth and throughput", Proc. SPIE 7010, 70103P (2008).

[4] Mawet, D., Serabyn, E., Liewer, K., Hanot, C., McEldowney, S., Shemo, D., O'Brien, N., "Optical Vector Vortex Coronagraphs using Liquid Crystal Polymers", Optics Express 17, 1902 (2009).
[5] Lyon, R. G., Clampin, M., Woodruff, R., et al., "Visible Nulling Coronagraphy for Exo-Planetary Detection and Characterization", IAU Colloq. 200: Direct Imaging of Exoplanets: Science & Techniques, 345 (2006).
[6] Krist, J., Belikov, R., Mawet, D., Moody, D., Pueyo, L., Shaklan, S., and Trauger, J., "Assessing the performance limits of internal coronagraphs through end-to-end modeling: Milestone results reports", available at http://exep.jpl.nasa.gov/technology.
[7] Krist, J., Moody, D., Mawet, D., Trauger, J., Belikov, R., Shaklan, S., Guyon, O., and Vanderbei, R., "End-to-end simulations of different coronagraphic techniques", Proc. SPIE 7440, 744016 (2009).
[8] Krist, J., Belikov, R., Mawet, D., Moody, D., Pueyo, L., Shaklan, S., and Trauger, J., "Assessing the performance limits of internal coronagraphs through end-to-end modeling: a NASA TDEM study", Proc. SPIE, 8151, 81510E (2011).
[9] Krist, J., "PROPER: an optical propagation library for IDL", Proc. SPIE 6675, 66750P (2007).
[10] Vanderbei, R., "Diffraction analysis of Two-Dimensional Pupil Mapping for High-Contrast Imaging", Astrophysical Journal 636, 528 (2006).
[11] Belikov, R., Kasdin, N., and Vanderbei, R., "Diffraction-based Sensitivity Analysis of Apodized Pupil-mapping Systems", Astrophysical Journal 652, 833 (2006).
[12] Pueyo, L, Shaklan, S., Krist, J., "Numerical propagator through PIAA optics," Proc. SPIE, 7440, 74400E (2009).
[13] Krist, J., Pueyo, L., and Shaklan, S., "Practical numerical propagation of arbitrary wavefronts through PIAA optics", Proc. SPIE 7731, 77314N (2010).
[14] Give'on, A., Kern, B., Shaklan, S., Moody, D., and Pueyo, L., "Broadband wavefront correction algorithm for high-contrast imaging systems", Proc. SPIE 6691, 66910A (2007)
[15] Abramowitz, M., and Stegun, I., "Handbook of Mathematical Functions", New York:Dover (1972).
[16] Soummer, R., Pueyo, L., Sivaramakrishnan, A., Vanderbei, R., "Fast computation of Lyot-style coronagraph propagation," Optics Express, 15, 15935 (2007).